Rotary bending fatigue analysis of shape memory alloys

Maede Hesami, Laurent Pino, Luc Saint-Sulpice, Vincent Legrand, Mahmoud Kadkhodaei, Shabnam Arbab-Chirani, Sylvain Calloch

Rotary bending fatigue analysis of shape memory alloys

Maede Hesami[1], Laurent Pino[2], Luc Saint-Sulpice[2], Vincent Legrand[2,3], Mahmoud Kadkhodaei[1], Shabnam Arbab Chirani[2] and Sylvain Calloch[3]

Abstract

In this work, a one-dimensional constitutive model is used to study rotary bending fatigue in shape memory alloy beams. The stress and strain distributions in a beam section are driven numerically for both pure bending and rotary bending to show the basic differences between these two loading types. In order to verify the numerical results, experiments are performed on NiTi specimens with an imposed bending angle using a bending apparatus. Since the specimens show significant stress plateau for forward and backward transformation in their stress–strain response, an enhanced stress–temperature phase diagram is proposed in which different slopes are considered for the start and finish of each transformation strip. In order to study low cycle fatigue of shape memory alloys during rotary bending, the stabilized dissipated energy is calculated from numerical solution. A power law for variations of the fatigue life with the stabilized dissipated energy is obtained for the studied specimens to predict their fatigue life. The numerical predictions of the present approach are shown to be in a good agreement with the experimental findings for rotary bending fatigue. Uniaxial tensile fatigue tests are further performed on the studied specimens to investigate effect of loading type on the fatigue lifetime.

Keywords

Rotary bending, fatigue, shape memory alloy, stabilized dissipated energy, phase diagram

Introduction

Shape memory alloys (SMAs) are an extraordinary group of materials that have been attracting much attention in recent years. Due to a reversible martensitic transformation, they can display the unusual properties of shape memory effect and superelasticity (pseudoelasticity). These unique properties enable them to be used in a wide range of medical (Duerig et al., 1999) and nonmedical (Van Humbeeck, 1999) applications. Among different kinds of SMAs, NiTi alloys have received a lot of attention in the medical industry because they combine high damping capacity with biocompatibility (Pelton, et al., 2013). Many SMA devices are subjected to cyclic loading which may well lead to fatigue. Therefore, characterizing the fatigue behavior of these materials in cyclic loading is overriding. So far, numerous fatigue experiments have been performed under uniaxial loading (Kang et al., 2012; Sameallah et al., 2015; Wilkes and Liaw, 2000; Yang et al., 2012). However, SMA components are generally subjected to other kinds of loading such as rotary bending in endodontic instruments (Plotino et al., 2009). In fact, when the instrument rotates freely in the tooth root canal, tension/compression cycles are generated at the point of maximum flexure until the fracture occurs.

Better understanding of the rotary bending fatigue (RBF) problem requires sufficient knowledge about uniaxial fatigue, in which the specimens undergo uniform stress and strain distribution over the cross section. Many experimental studies (McNichols et al., 1981; Melton and Mercier, 1979; Prahlad and Chopra, 2003) focused on uniaxial fatigue of SMAs and evaluated the effect of transformation temperature, strain amplitude, and strain rate on the fatigue life of these materials. In a theoretical framework, Moumni et al. (2005) showed that the amount of stabilized dissipated energy under uniaxial loading is related to the number of cycles for failure in an SMA. Sameallah et al. (2014)

[1]Department of Mechanical Engineering, Isfahan University of Technology, Isfahan, Iran
[2]ENI Brest, FRE CNRS 3744, IRDL, Brest, France
[3]ENSTA Bretagne, FRE CNRS 3744, IRDL, Brest, France

Corresponding author:
Mahmoud Kadkhodaei, Department of Mechanical Engineering, Isfahan University of Technology, Isfahan 8415683111, Iran.
Email: kadkhodaei@cc.iut.ac.ir

proposed a direct numerical approach for determination of stabilized dissipated energy of SMAs under cyclic tensile loadings as a function of maximum and minimum applied stresses as well as loading frequency.

In RBF framework, Tobushi et al. (1998) experimentally investigated the influence of strain amplitude and rotational speed on fatigue life of a rotary bent wire in different environments. Eggeler et al. (2004) studied the structural and functional fatigue of pseudoelastic NiTi wires subjected to RBF. For functional fatigue, they studied the influence of wire diameter and rotational speed by deriving strain–life curves. Siredey et al. (2005) focused on RBF failure of CuAlBe SMA under various imposed strains in a special circular bending apparatus and compared the lifetime with that of NiTi. In addition, they performed microstructural analysis on damage during cycling and showed that the quality of the surface is of great importance on the fatigue lifetime. Pelton et al. (2013) investigated the fatigue properties of medical-grade Nitinol under 0.5%–10% strain amplitudes for low cycle fatigue (LCF) and high cycle fatigue (HCF). They used a guided rotary bend tester which simulates the root canal for endodontic files. In addition, finite element (FE) analysis was used to illustrate strain distributions across the wire. Rahim et al. (2013) used a computer-controlled test rig which efficiently allows to collect fatigue data using RBF of NiTi alloys. They also employed fractography to better understand the role of inclusions during fatigue in pseudoelastic NiTi. In all of the mentioned experimental studies, the strain amplitude has been estimated by a simplified pure bending model, and the influence of rotation and the repeated tension–compression cycling has been neglected. Moreover, although practical applications of RBF are in complex geometries, wire is considered to simplify the RBF problems. Wagner and Eggeler (2006) analytically presented a mechanical description for distributions of stress and strain during pseudoelastic bending rotation. They showed differences between pure bending and bending rotation for a bilinear material model with symmetric tension–compression behavior. However, to the authors' knowledge, none of the available studies present a theoretical framework for predicting fatigue life of an SMA under rotary bending loading.

In this article, the one-dimensional constitutive model proposed by Brinson (1993) is adopted to study RBF of a bent SMA beam. A detailed mechanical analysis of the stress and strain states is proposed in an SMA beam subjected to bending rotation and pure bending. The transformation is experimentally found to take place very gradually for the studied NiTi specimens. Hence, an enhanced stress–temperature phase diagram is proposed in which different slopes for the start and finish of transformation strips are taken into account. The stabilized dissipated energy is obtained from the numerical model, and the fatigue life is predicted based on the approach proposed by Moumni et al. (2005). A good agreement is seen between the numerical and experimental findings for RBF of SMA beams. Therefore, a simplified model based on material parameters of uniaxial tensile test is proposed to investigate the fatigue life of rotary bending SMA wires with a reasonable accuracy. In addition, the RBF results are compared with experimental and numerical tensile fatigue data for the studied samples. Accordingly, different fatigue coefficients are obtained based on loading type.

Modeling

In the present work, Brinson (1993) approach is used for constitutive modeling. In this model, martensite volume fraction, ζ, is separated into two parts as follows

$$\zeta = \zeta_s + \zeta_T \tag{1}$$

where ζ_T and ζ_s represents the temperature- and the stress-induced martensite volume fractions, respectively.

Based on Brinson and Huang's (1996) approach, the thermal part of strain is negligible in comparison with the transformation part. Consequently, the strain can be separated into elastic part and transformation part

$$\varepsilon = \varepsilon^e + \varepsilon^{tr} = \frac{\sigma}{E} + \varepsilon^* \zeta_s \tag{2}$$

where ε^* is the maximum recoverable strain of the material. Young's modulus is expressed by the Reuss scheme as follows

$$E(\zeta) = \left(\frac{1-\zeta}{E_A} + \frac{\zeta}{E_M} \right)^{-1} \tag{3}$$

in which E_A and E_M are Young's moduli of pure austenite and martensite, respectively.

Based on Sameallah et al., (2015) model, an enhanced stress–temperature phase diagram can be used in which different slopes are considered for the start and finish of the transformation strips. In the present work, according to Figure 1, four lines with different slopes are considered. The stress- and temperature-induced parts of the martensite volume fraction for pseudoelastic alloy ($T > A_f$) are determined as follows

$$\begin{aligned} &\text{For } \dot{\sigma} > 0 \text{ and } T > M_s \text{ and } C_{MS}(T - M_s) < \sigma < C_{MF}(T - M_f): \\ &\zeta_s = \frac{1-\zeta_{s0}}{2} \cos \\ &\left\{ \frac{\pi}{C_{MS}(T - M_s) - C_{MF}(T - M_f)} \left[\sigma - C_{MF}(T - M_f) \right] \right\} \\ &+ \frac{1+\zeta_{s0}}{2} \end{aligned} \tag{4}$$

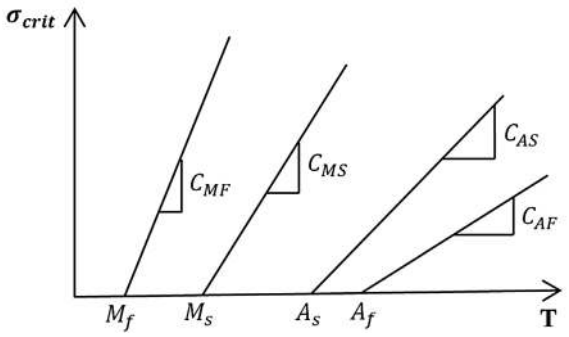

Figure 1. The proposed enhanced pseudo phase diagram.

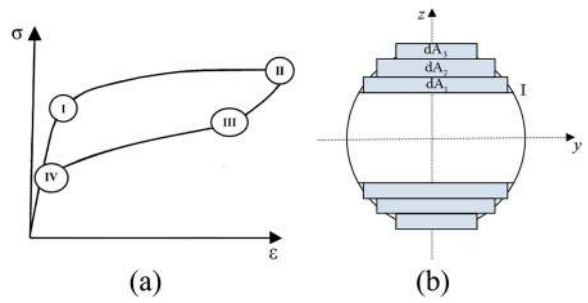

Figure 2. (a) Stress–strain curve for a superelastic SMA and (b) cross section of a bent beam.

$$\zeta_T = \frac{1-\zeta_s}{1-\zeta_{s0}}\zeta_{T0} \tag{5}$$

For $\dot{\sigma}<0$ and $T>A_s$ and $C_{AF}(T-A_f)<\sigma<C_{AS}(T-A_s)$:

$$\zeta_S = \frac{\zeta_0}{2}\left\{1+\cos\left(\frac{\pi}{C_{AF}(T-A_f)-C_{AS}(T-A_s)}(\sigma-C_{AS}(T-A_s))\right)\right\} \tag{6}$$

$$\zeta_T = \frac{\zeta_{T0}}{2}\left\{1+\cos\left(\frac{\pi}{C_{AF}(T-A_f)-C_{AS}(T-A_s)}(\sigma-C_{AS}(T-A_s))\right)\right\} \tag{7}$$

In the relations above, ζ_{s0} and ζ_{T0} are the stress- and temperature-induced martensite volume fractions prior to the current transformation, respectively. M_s, M_f, A_s, and A_f are the martensite start, martensite finish, austenite start, and austenite finish temperatures, respectively. The constants C_{MS}, C_{MF}, C_{AS}, and C_{AF} are material properties which describe the slope of martensite start, martensite finish, austenite start, and austenite finish strips in the stress–temperature phase diagram shown in Figure 1. It is worth mentioning that considering four different slopes enables gradual forward and backward transformation of the studied specimens under uniaxial tensile tests.

In order to achieve the bending moment in the critical section of a bent wire, a thorough investigation on the stress and the strain distributions during bending rotation and pure bending experiments is presented in the following sections.

Pure bending model

Pure bending is a load case where an originally straight wire is bent into a curved shape and is unbent to return to its initial configuration. In this section, one-dimensional constitutive equation based on the Brinson approach is used to determine the stress and strain distributions in a beam section. The beam section is considered in y-z plane (Figure 2(b)) and bending moment, M_y, is applied for bending the beam. Strain, ε, is a linear function of distance from the bending axis, z (more information is provided in Appendix 1)

$$\varepsilon = az \tag{8}$$

where a is the curvature. In the loading cycle, when a beam is bent, the cross section is divided into elastic and inelastic parts (Figure 2(b)). By increasing the distance of each point from the neutral axis ($z = 0$), strain and stress will increase until they reach the transformation region. (I) is the boundary between elastic and inelastic regions (Figure 2(a)) which can be derived as follows. Note that subscript p indicates the pure bending loading in all of the following relations

$$\varepsilon = \varepsilon_I \rightarrow az_{IP} = \varepsilon_I \rightarrow z_{IP} = \frac{\sigma_I}{aE_A} \tag{9}$$

where σ_I is the transformation start stress and ε_I is the corresponding strain. The bending moment for elastic region is determined as

$$M_e = 2\int_0^{z_{IP}} E_A a z^2 \sqrt{4\left(\left(\frac{d}{2}\right)^2 - z^2\right)}\cdot dz \tag{10}$$

where d is the wire diameter. When the distance of each point in the section exceeds z_{IP}, the forward transformation begins. In this situation, the non-linear constitutive equations in the transformation regions cannot be solved analytically. Consequently, integration elements are considered for numerical solution as shown in Figure 2(b). Finally, the bending moment of every element for loading cycle can be calculated as follows. The subscript i denotes the number of elements in the inelastic region

$$M_i = 2\cdot\sigma_i\cdot dA_i\cdot z_i \tag{11}$$

where dA_i is the integration element of inelastic region based on Figure 2(b), and σ_i is the stress value of the corresponding element.

During unloading, when a bent beam is unbent to its straight shape, the inelastic region of the section can experience different states depending on distance from the neutral axis, z_i. The boundaries of each state are

$$\begin{cases} \sigma_{III} - \sigma_{II} = E_{IIP}(\varepsilon - \varepsilon_{IIP}) \\ z = \frac{\varepsilon}{a} \end{cases} \rightarrow z_{IIIP} = \frac{\sigma_{II} - \sigma_{III}}{E_{IIP}(a - a_{IIP})} \tag{12}$$

$$z_{IVP} = \frac{\sigma_{IV}}{aE_A} \tag{13}$$

in which $\sigma_{II}, \sigma_{III}$, and σ_{IV} are stresses in points (*II*), (*III*), and (*IV*) in Figure 2(a). In fact, z_{IIIP} is the boundary between elastic unloading and backward transformation, and z_{IVP} separates final elastic region from transformation region. E_{IIP} is Young's modulus in region *II* for elastic unloading in each element.

Finally, the total bending moment in unloading cycle can be defined as

$$M = 2\int_0^{z_{IUP}} E_A a z^2 \sqrt{4\left(\left(\frac{d}{2}\right)^2 - z^2\right)} \cdot dz + \sum_{i=1}^{n} M_i \tag{14}$$

where z_{IUP} is the boundary between elastic and inelastic unloading region based on equation (15) and n is the number of elements in the inelastic region

$$\varepsilon = \varepsilon_{\mathrm{I}} \rightarrow a_{IIP} z_{IUP} = \varepsilon_{\mathrm{I}} \rightarrow z_{IUP} = \frac{\sigma_I}{a_{IIP} E_A} \tag{15}$$

Rotary bending model

As previously discussed, in this load case, an originally straight beam is bent into a curved shape and is subsequently forced to rotate around its longitudinal axis. Based on the method proposed by Wagner and Eggeler (2006), a polar coordinate system (radius r and angle θ) is used to track the positions of all points in the cross section. Symmetric tension–compression response is considered for the material. Consequently, half of the SMA beam section which is subjected to tension is adequate for analyzing (Figure 3(b)). On the basis of the stress–strain behavior illustrated in Figure 3(a), the stress state can be determined based on the four boundaries shown in Figure 3(b). When the wire rotates, each material point follows a circular path. By increasing θ from 0° to 90°, the material experiences increasing tensile strain. Between the zero strain line ($z = 0$) and position (*I*), the deformation is purely linear–elastic. As the material rotates from position (*I*) to position (*II*), it passes through the tensile loading plateau. At $\theta = 90°$ (position (*II*)), the maximum tensile strain is reached and unloading starts. As the point moves from positions (*II*) to (*III*), it passes through the elastic unloading part. At position (*III*), the material enters the unloading plateau. From point (*IV*), the deformation is purely linear–elastic until $\theta = 180°$. The material subsequently passes through similar steps in compression, and the rotation is completed when $\theta = 360°$.

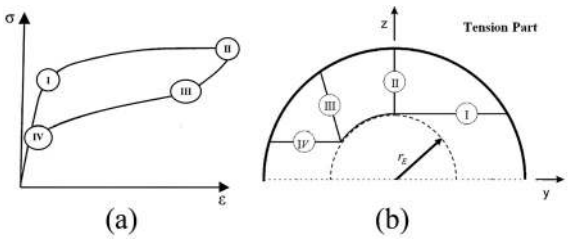

Figure 3. (a) Stress–strain diagram with the characteristic points. (b) Schematic representation of the stress distribution in half of the cross section of a pseudoelastic wire subjected to bending rotation.

Therefore, line (*I*) separates the elastic loading regime (below the line (*I*)) from the pseudoelastic loading plateau. Line (*II*) is the boundary between the loading plateau and the elastic unloading region. Line (*III*) separates the elastic unloading part from unloading plateau region. Finally, the boundary between the unloading plateau and the last elastic region is represented by line (*IV*). The mathematical calculations of these lines, based on Brinson (1993) approach, are presented as follows

$$\begin{aligned} \varepsilon = \varepsilon_I \rightarrow az = \varepsilon_I \rightarrow a(r\,\sin\theta_I) \\ = \frac{\sigma_I}{E_A} \rightarrow \theta_I(r) = \sin^{-1}\frac{\sigma_I}{E_A r a} \end{aligned} \tag{16}$$

$$\theta_{II}(r) = 90° \tag{17}$$

$$a(r\,\sin\theta_{III}) = \frac{\sigma_{III}}{E_{II}} \rightarrow \theta_{III}(r) = \sin^{-1}\frac{\sigma_{III}}{E_{II} r a} \tag{18}$$

$$a(r\,\sin\theta_{IV}) = \frac{\sigma_{IV}}{E_A} \rightarrow \theta_{IV}(r) = \sin^{-1}\frac{\sigma_{IV}}{E_A r a} \tag{19}$$

A critical radial distance r_E (see Figure 3(b)) is the maximum radius of circle in which no martensitic transformation occurs; therefore, every point close to the center of the wire and below r_E only experiences purely elastic tension–compression cycles. Therefore, r_E can be calculated as follows

$$a r_E\,\sin(90°) = \frac{\sigma_I}{E_A} \rightarrow r_E = \frac{\sigma_I}{E_A a} \tag{20}$$

The elastic bending moment can be analytically obtained by polar integration, but the inelastic part needs numerical calculation. Thus, FEs are used to calculate bending moment as shown in Figure 4. Accordingly, the total bending moment can be calculated as follows

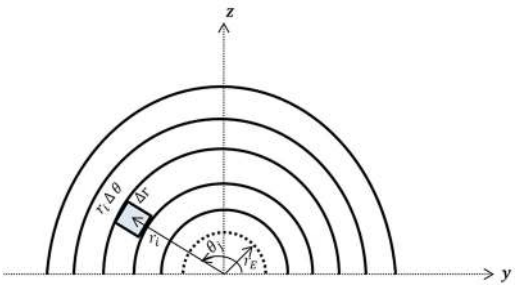

Figure 4. A typical element for numerical solution in rotary bending.

$$M = 2\int_0^{r_e}\int_0^{\pi} E_A a(r\sin\theta)^2 r d\theta dr + \sum_{i=1}^{n_r}\sum_{j=1}^{n_\theta} 2\sigma_{ij}\cdot r_i\Delta\theta\cdot\Delta r\cdot r_i\sin\theta_j \tag{21}$$

Fatigue life

Based on Moumni et al.'s (2005) approach, the amount of stabilized dissipated energy is related to the number of cycles for failure, that is, the fatigue life of an SMA. From the internal forces viewpoint, the stress and strain can be integrated for each integration section point so the amount of dissipated energy can be calculated as follows

$$W_d = \int_V \sigma\, d\varepsilon dV \tag{22}$$

Another approach for deriving the dissipated energy in pure bending is calculating bending moment in each bending angle (φ)

$$W_d = \int M\, d\varphi \tag{23}$$

It should be noted that in the rotary bending model, φ is constant during the time so only the first approach is valid to calculate the dissipated energy.

Experiments

Material characterization

In this study, all the utilized specimens have been obtained from two NiTi wires (1 and 1.2 mm diameter) with the composition of Ni (50.8 wt%) and Ti (49.2 wt%). Three types of samples are used for different tests: (1) dogbone samples for uniaxial tensile tests, (2) diabolo samples for RBF tests and uniaxial tensile fatigue tests, and (3) straight samples for estimation of tension–compression asymmetry.

Figure 5 shows Differential Scanning Calorimetry (DSC) analysis for evaluating the transformation temperatures of the considered wires. The occurrence of two-stage phase transformations is clearly visible. The extra peaks during cooling (for sample 1) and heating (for sample 2) are assumed to be caused by Rhombohedral-phase (R-phase) transition which is common in NiTi alloys.

Uniaxial tensile tests were conducted on two kinds of NiTi dogbone samples with different diameters. The schematic figure of the samples and their dimensions are shown in Figure 6. The tests were realized in quasi-static conditions ($\dot{\varepsilon} = 10^{-5}\,s^{-1}$) at different temperatures (35°C, 50°C, and 65°C) to obtain austenite and martensite Young's moduli, maximum recoverable strain, and the phase diagram parameters. Another test at 20°C is carried out for validation of the model as shown in Figure 9.

RBF tests

Rotary bending tests were performed using two diabolo samples (Figure 7) which are geometrically different from characterization test samples (Figure 6) but have been obtained from the same NiTi wires. In fact, compared to the tensile specimens, greater curvature in the middle of the fatigue samples enables us to have failure at the center of the sample not at the boundary edges.

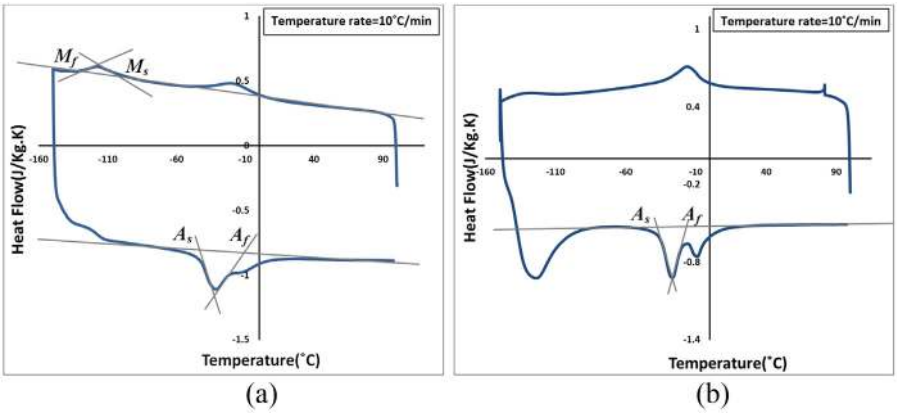

Figure 5. DSC analysis for the evaluation of transformation temperatures: (a) sample 1 and (b) sample 2.

Table 1. Material properties of NiTi for enhanced phase diagram.

	E_A (MPa)	E_M (MPa)	ε^*	M_s (°C)	M_f (°C)	C_{AS} (MPa K^{-1})
Sample 1	64,360	22,054	0.06	–85	–120	6.5
Sample 2	67,340	26,200	0.06	–65.2	–81.5	7.4
	C_{AF} (MPa K^{-1})	C_{MS} (MPa K^{-1})	C_{MF} (MPa K^{-1})	A_f (°C)	A_s (°C)	
Sample 1	8	6.8	5.82	–10.51	–45.63	
Sample 2	6.41	7.5	7.9	–17	–34	

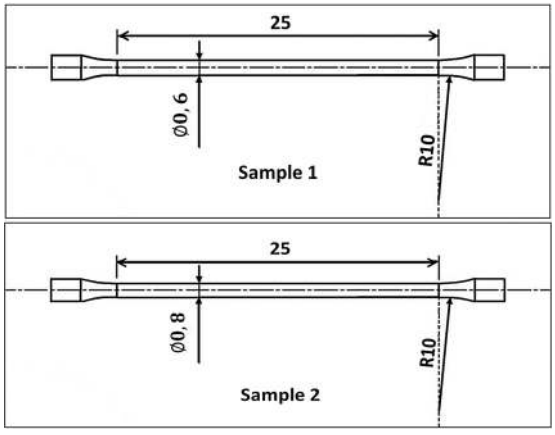

Figure 6. Geometries of NiTi tensile dogbone samples for material characterization.

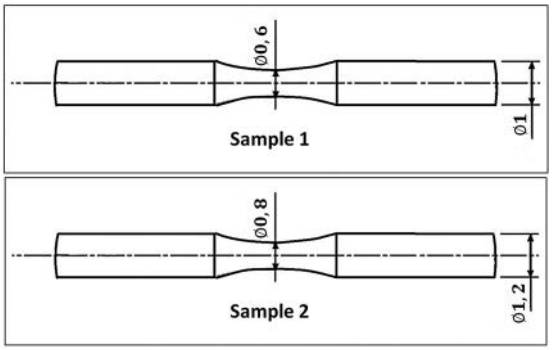

Figure 7. NiTi diabolo samples for fatigue tests.

The employed bending apparatus is shown in Figure 8. It consists of three main components:

1. Motor: it forces the beam to rotate at a constant angular velocity (400 r/min in this study) by transmitting rotation to the end of the beam. In fact, one end of the sample is fixed in the motor while the other end is free to rotate.
2. Torque sensor: it is to measure the bending torque (0.2 N m range and 0.8 mV/V sensibility). The sensor realizes the moment measurement at the middle of the sample.
3. Bending actuator: it is used to select the angle of bending. The sensors are mounted between the bending actuator and the support of the free jaw.

Uniaxial tensile fatigue tests

Tensile fatigue tests are performed by a Bose ElectroForce 3330 system on the similar diabolo samples used in RBF (shown in Figure 7) under different stress amplitudes (700, 725, 775, and 800 MPa) to determine the strength-number of cycles (S-N) curve and to predict the fatigue life. All the tests are carried out at the frequency of 30 Hz and the constant ambient temperature of 20°C (which is higher than the austenite finish temperature) to ensure the appearance of pseudoelastic response.

Results and discussion

Table 1 shows the material parameters obtained from the characterizing tensile tests and the DSC analysis for dogbone samples 1 and 2. To ensure the accuracy of the estimated material parameters, typical numerical uniaxial stress–strain responses of the samples are compared with empirical results in Figure 9. Good agreement between the empirical and analytical results verifies the reported material parameters.

In bending tests, the moment–angle curves can be developed from the empirical results using torque sensor and bending actuator. Using the numerical solution, bending moment–curvature response is calculated. To compare numerical results with empirical ones, bending angle–curvature relation must be determined. To do this, since such a relation is more related to geometric constraints than to the material response, FE simulation is performed in ABAQUS for a typical elasto-plastic material. Since SMA constitutive equations are not defined in ABAQUS, the SMA stress–strain response is reproduced in the form of an elasto-plastic behavior in the software. Therefore, the austenite Young' modulus is assigned for elastic response and the piecewise approximation of the transformation region is used for the plastic part. Figure 10(a) shows the schematic of pure bending problem. One end of the specimen is constrained with the free jaw and the other end

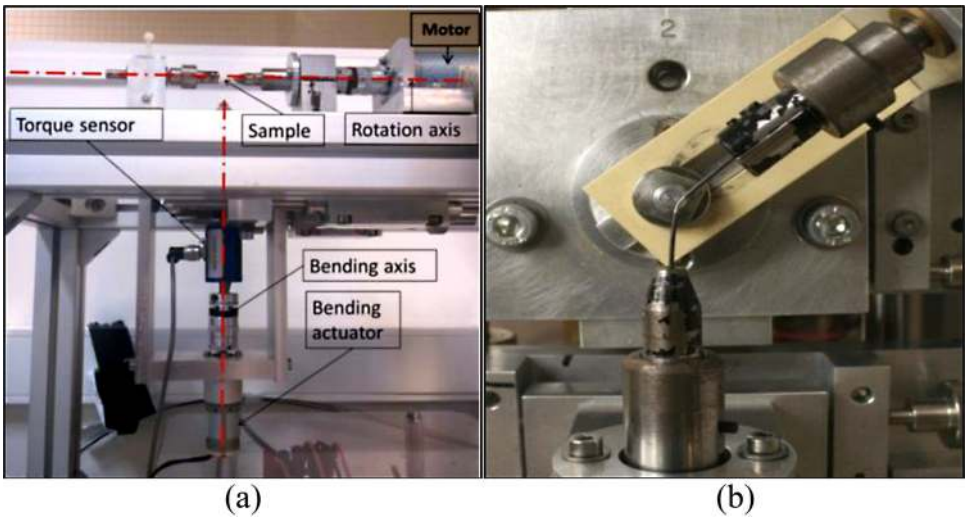

Figure 8. (a) Experimental setup for rotary bending fatigue and (b) upside view of diabolo sample in the machine.

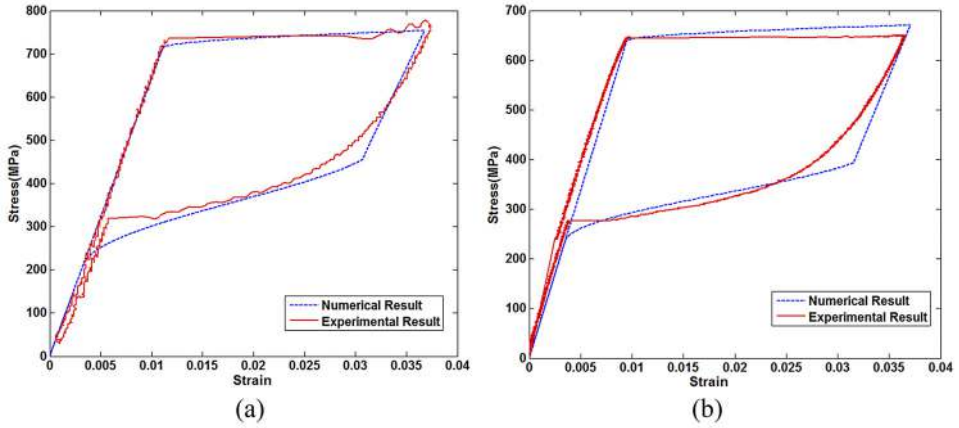

Figure 9. Comparison of numerical and experimental results in the tensile test for (a) diabolo sample 1 and (b) diabolo sample 2.

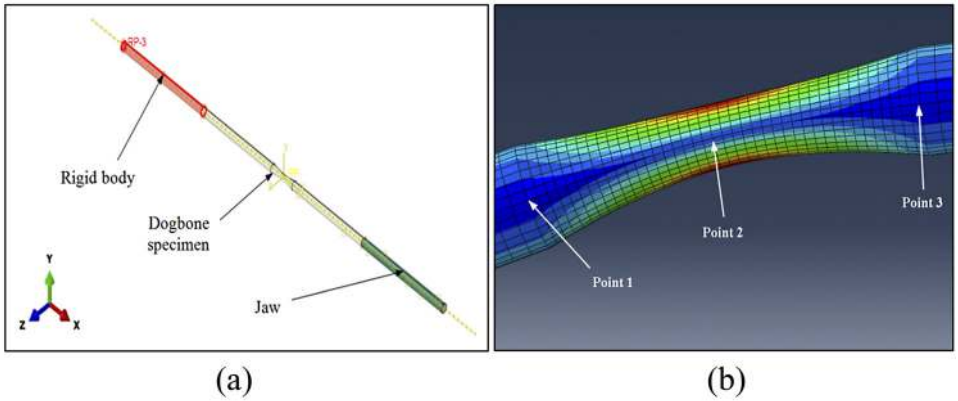

Figure 10. (a) Bending simulation by finite element method to obtain angle–curvature relations and (b) the three points used for calculating curvature.

is rigidly fixed. A reference point is located at the center of the specimen and is coupled to the free jaw rotation. After applying bending angle to the reference point, the curvature is calculated for each bending angle by three-point coordinates located at the start, center, and the end of the middle arc as shown in Figure 10(b). Finally,

Table 2. Phase diagram coefficients after considering tension–compression asymmetry.

	C_{MF}^{-} (MPa K^{-1})	C_{MF}^{+} (MPa K^{-1})	C_{MS}^{-} (MPa K^{-1})	C_{MS}^{+} (MPa K^{-1})
Sample 1	6.69	5.82	11.56	6.8
Sample 2	9.48	7.9	9	7.5

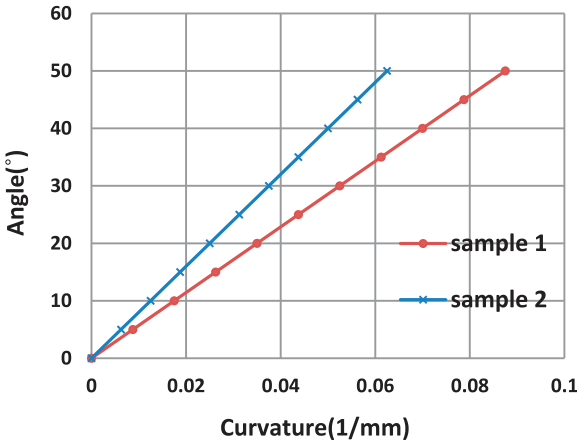

Figure 11. Bending angle–curvature relation obtained by finite element simulation.

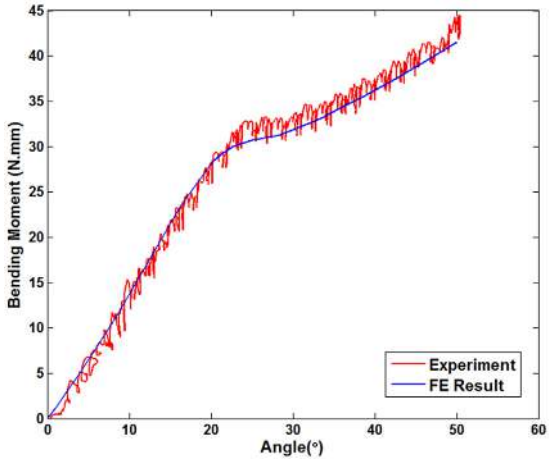

Figure 12. Comparison between experimental result and FE simulation for sample 1.

the linear bending angle–curvature relation is obtained for each specimen as shown in Figure 11.

To assure the accuracy of the simulation, bending moment–angle curve is derived in ABAQUS. Figure 12 compares the derived FE curve with experiment. Good agreement between FE result and empirical finding can validate the simulation and the utilized elasto-plastic material.

After determination of the bending angle–curvature relation, the simulation results of the simplified model are compared with the experimental findings for the two samples as shown in Figure 13. The considerable difference between analytical and experimental results has two main origins: (1) stress concentration in the middle of diabolo sample and (2) asymmetric behavior of material in tension and compression which does not affect the elastic region. These factors must then be introduced in the present numerical model.

In order to consider the effect of each factor separately, a straight sample is used (Figure 14(a)) to avoid stress concentration. Based on the approaches proposed by Karamooz et al. (2015) and Mehrabi et al. (2014), different material parameters are considered for tension (+) and compression (–) regions. The values presented in Table 2 are determined using reverse identification. Figure 14 illustrates that the asymmetric model yields results with an acceptable accuracy compared to the empirical observations for the uniform specimen.

For the second factor, one must define equation (24) as a stress concentration factor (SCF). Since this factor is a function of geometry, loading type, and the material, experiment is the best method to take its effect into account. Four bending tests were performed in different angles (25°, 30°, 35°, and 40°) for each specimen to estimate SCF (more information is provided in Appendix 2)

$$K_f = \frac{\sigma_{\max}}{\sigma_{\text{nominal}}} \tag{24}$$

Finally, the SCF values of 1.8 and 2.2 are obtained for diabolo sample 1 and diabolo sample 2, respectively. Figure 15 shows the effect of applying SCF in asymmetric numerical model for the two samples. The illustrated reasonable agreement between the empirical and numerical results verifies these estimated factors.

In Figure 16, the empirical results are compared with theoretical predictions in two different load cases: pure bending (loading cycle) and rotary bending. The good agreements between the curves can verify the presented numerical scheme for the both loading types. For the same angle of bending, it is seen that the amount of moment in pure bending is higher than that in rotary bending; because, in bending rotation, the unloading plateaus decrease the amount of stress value for each angle.

For fatigue analysis, the first stress–strain curve is considered to be the stabilized response of the alloy by neglecting temperature variations in the specimen.

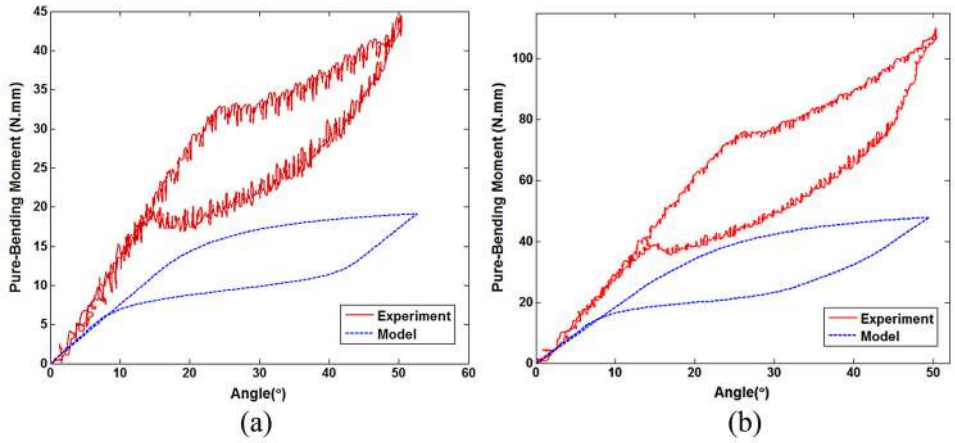

Figure 13. Comparison between momentangle responses obtained by the numerical model and experiment: (a) dogbone sample 1 and (b) dogbone sample 2.

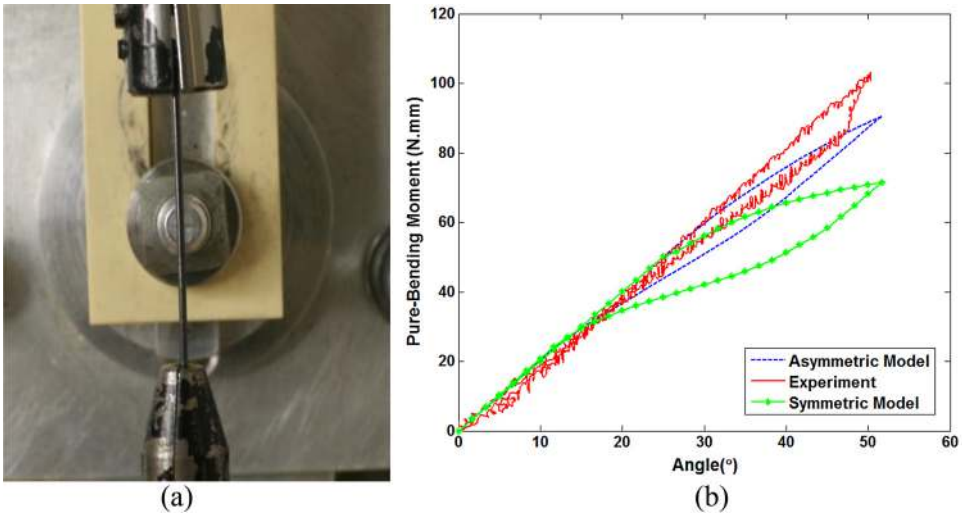

Figure 14. Illustration of (a) the utilized straight sample 1, and (b) its moment angle-response.

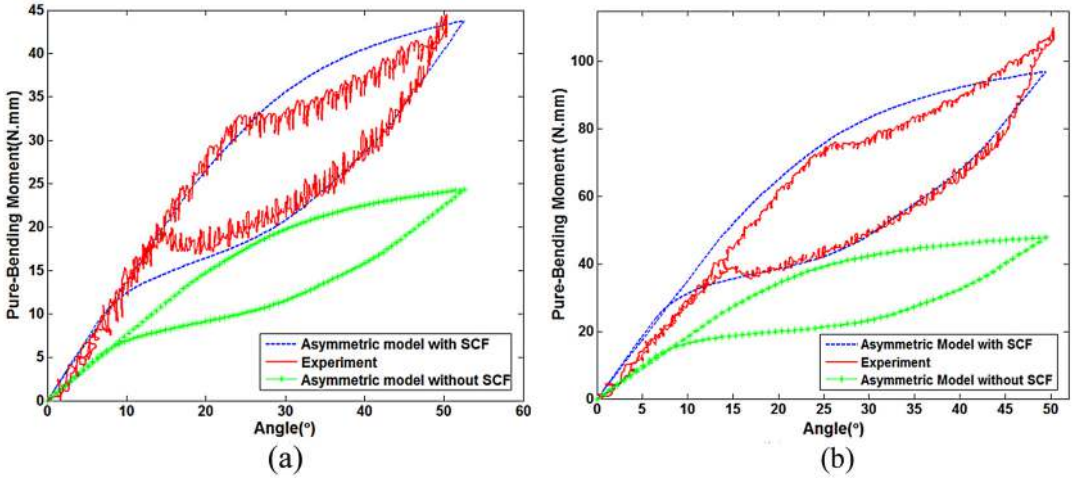

Figure 15. Comparison between modified asymmetric models (with SCF and without SCF) and experiment for (a) diabolo sample 1 and (b) diabolo sample 2.

Table 3. Dissipated energy coefficients.

Sample type	K_w (mJ)	α	Loading type
Sample 1	547.64	–0.204	Uniaxial tensile fatigue
Sample 1	877.12	–0.841	Rotary bending fatigue
Sample 2	3451.3	–0.358	Uniaxial tensile fatigue
Sample 2	517.77	–0.731	Rotary bending fatigue

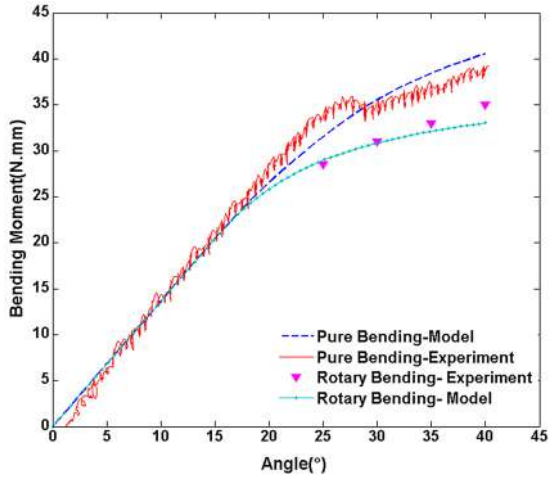

Figure 16. Comparison between the numerical and experimental results for diabolo sample 1 in the two studied loading cases.

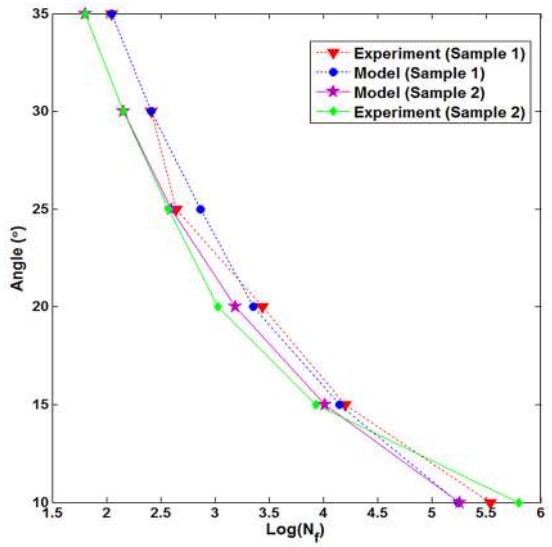

Figure 17. Comparison between the numerical and empirical fatigue lifetimes of two samples in RBF test at 400 r/min.

Consequently, the stabilized dissipated energy can be easily calculated using equations (22) for uniaxial tensile fatigue and RBF. Using approach proposed by Moumni et al. (2005), the fatigue life can be predicted by equation (25). Table 3 shows dissipated energy coefficients for two types of loading (tension and rotary bending) in the two studied samples. Note that the constant coefficients in each sample are calculated from experiment. As is seen, loading type affects the coefficients and, in turn, the fatigue lifetime

$$W_d = K_w \times N_f{}^{\alpha} \tag{25}$$

Figure 17 shows lifetime of the two samples in different rotary bending angles. It is worth mentioning that these curves indicate LCF of the specimens so rupture occurs early at relatively low amounts of N_f and the fatigue lifetime strongly depends on rotary bending angle. Good agreement between numerical and empirical results for two samples verifies the numerical solution. These curves can also indicate the size effect in LCF lifetime. Similar to observations in HCF, a smaller wire diameter causes a longer fatigue lifetime. According to the numerical results, the size effect is more pronounced for larger bending angles. For instance, when the bending angle is 10°, the elastic response dominates the material section. Therefore, the amounts of dissipated energy for the two samples are low and very close to each other. This is why almost the same lifetimes are predicted.

For uniaxial tensile fatigue, the resultant S-N curves obtained from the model and the experiment for different stress amplitudes are shown in Figure 18. The reported coefficients for uniaxial tensile fatigue (Table 3) are verified according to the good agreement between numerical and experimental results in this figure (maximum error in sample 1 is 2.94% and in sample 2 is 1.96%).

Figure 19 shows variations of the numerically predicted fatigue lifetime with dissipated energy for the two loading types. As is seen, for a specified amount of dissipated energy, different lifetimes are obtained for these two different loading types. Therefore, beside material properties and dimensions, loading type does affect the fatigue properties of SMAs.

Conclusion

The present study focuses on basic understanding of RBF in a pseudoelastic SMA beam. An enhanced stress–temperature phase diagram is presented for cases

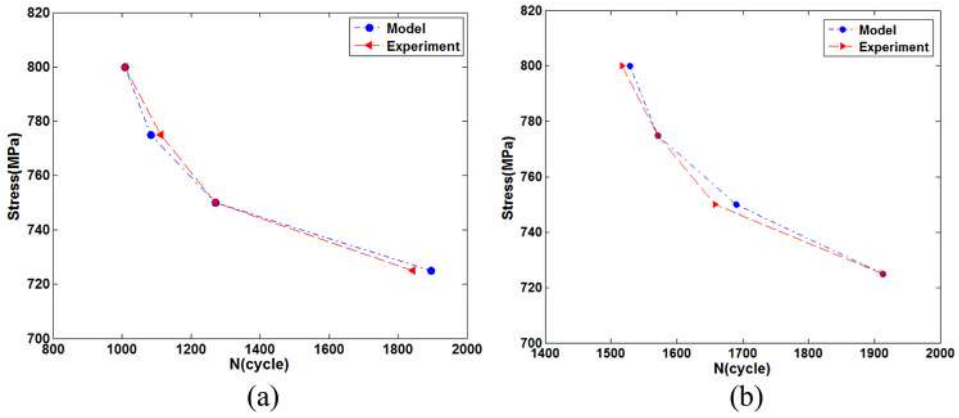

Figure 18. Comparison between the numerical and empirical S-N curves in uniaxial tensile fatigue for (a) sample 1 and (b) sample 2.

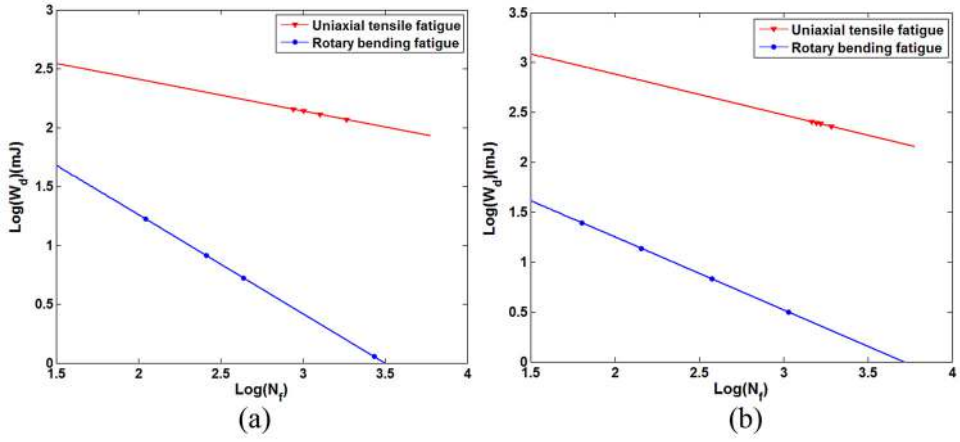

Figure 19. Comparison of functional fatigue behavior between two types of loading: (a) sample 1 and (b) sample 2.

where gradual forward and reverse transformations occur, and a one-dimensional constitutive model is utilized to determine moment–curvature response. Different stress and strain states are shown to appear in pure bending and bending rotation. For fatigue analysis, the lifetime is expressed as a function of stabilized dissipated energy. By studying tensile and bending fatigue, it is shown that loading type affects the fatigue lifetime of an SMA so that different amounts of lifetime for a specified amount of dissipated energy is obtained for different types of loading. The expected size effect on the fatigue lifetime is also confirmed in this work. Several experiments are performed, and the numerical predictions are shown to be in reasonable agreements with empirical findings indicating accuracy of the presented approach.

Declaration of conflicting interests

The author(s) declared no potential conflicts of interest with respect to the research, authorship, and/or publication of this article.

Funding

This work has been supported by Center for International Scientific Studies & Collaboration (CISSC) and French Embassy in Tehran.

References

Brinson LC (1993) One-dimensional constitutive behavior of shape memory alloys: thermomechanical derivation with non-constant material functions and redefined martensite internal variable. *Journal of Intelligent Material Systems and Structures* 4(2): 229–242.

Brinson LC and Huang MS (1996) Simplifications and comparisons of shape memory alloy constitutive models. *Journal of Intelligent Material Systems and Structures* 7(1): 108–114.

Duerig TW, Pelton A and Stöckel D (1999) An overview of nitinol medical applications. *Materials Science and Engineering* 273: 149–160.

Eggeler G, Hornbogen E, Yawny A, et al. (2004) Structural and functional fatigue of NiTi shape memory alloys. *Materials Science and Engineering* 378(1): 24–33.

Kang G, Kan Q, Yu C, et al. (2012) Whole-life transformation ratcheting and fatigue of super-elastic NiTi Alloy under uniaxial stress-controlled cyclic loading. *Materials Science and Engineering* 535: 228–234.
Karamooz Ravari M, Kadkhodaei M and Ghaei A (2015) Effects of asymmetric material response on the mechanical behavior of porous shape memory alloys. *Journal of Intelligent Material Systems and Structures* 27: 1687–1701.
McNichols JL Jr, Brookes PC and Cory JS (1981) NiTi fatigue behavior. *Journal of Applied Physics* 52(12): 7442–7444.
Mehrabi R, Kadkhodaei M and Elahinia M (2014) Constitutive modeling of tension-torsion coupling and tension-compression asymmetry in NiTi shape memory alloys. *Smart Materials and Structures* 23(7): 075021.
Melton KN and Mercier O (1979) The effect of the martensitic phase transformation on the low cycle fatigue behaviour of polycrystalline NiTi and CuZnAl alloys. *Materials Science and Engineering* 40(1): 81–87.
Moumni Z, Van Herpen A and Riberty P (2005) Fatigue analysis of shape memory alloys: energy approach. *Smart Materials and Structures* 14(5): S287.
Pelton AR, Fino-Decker J, Vien L, et al. (2013) Rotary-bending fatigue characteristics of medical-grade Nitinol wire. *Journal of the Mechanical Behavior of Biomedical Materials* 27: 19–32.
Plotino G, Grande NM, Cordaro M, et al. (2009) A review of cyclic fatigue testing of nickel-titanium rotary instruments. *Journal of Endodontics* 35(11): 1469–1476.
Prahlad H and Chopra I (2003) Development of a strain-rate dependent model for uniaxial loading of SMA wires. *Journal of Intelligent Material Systems and Structures* 14(7): 429–442.
Rahim M, Frenzel J, Frotscher M, et al. (2013) Bending rotation HCF testing of pseudoelastic Ni-Ti shape memory alloys. *Material wissenschaft und Werkstofftechnik* 44(7): 633–640.
Sameallah S, Kadkhodaei M, Legrand V, et al. (2015) Direct numerical determination of stabilized dissipated energy of shape memory alloys under cyclic tensile loadings. *Journal of Intelligent Material Systems and Structures* 26(16): 2137–2150.
Sameallah S, Legrand V, Saint-Sulpice L, et al. (2014) A comprehensive energy approach to predict fatigue life in CuAlBe shape memory alloy. *Smart Materials and Structures* 24(2): 025004.
Siredey N, Hautcoeur A and Eberhardt A (2005) Lifetime of superelastic Cu-Al-Be single crystal wires under bending fatigue. *Materials Science and Engineering* 396(1): 296–301.
Tobushi H, Hachisuka T, Hashimoto T, et al. (1998) Cyclic deformation and fatigue of a TiNi shape-memory alloy wire subjected to rotating bending. *Journal of Engineering Materials and Technology* 120(1): 64–70.
Van Humbeeck J (1999) Non-medical applications of shape memory alloys. *Materials Science and Engineering* 273: 134–148.
Wagner MFX and Eggeler G (2006) Stress and strain states in a pseudoelastic wire subjected to bending rotation. *Mechanics of Materials* 38(11): 1012–1025.
Wilkes KE and Liaw PK (2000) The fatigue behavior of shape-memory alloys. *Journal of the Minerals, Metals & Materials Society* 52(10): 45–51.
Yang S, Dui G and Liu B (2012) Modeling of rate-dependent damping capacity of one-dimensional superelastic shape memory alloys. *Journal of Intelligent Material Systems and Structures* 24: 431–440.

Appendix 1

The negligible effect of asymmetry in tension–compression behavior on strain equation is studied here. Considering asymmetric response, strain equation is modified to

$$\varepsilon = az + c \tag{26}$$

c is the asymmetric coefficient which causes the neutral axis to be shifted. However, the amount of axial force should remain zero. Consequently, to determine the amount of c, the following equation of equilibrium must be satisfied

$$F_{Axial} = \int \sigma \times dA = 0 \tag{27}$$

Figure 20 shows the effect of asymmetric coefficient (c) for five different bending angles in the straight sample subjected to pure bending. As is seen, this coefficient has a negligible effect on the results since maximum error in the predicted moment occurs for the angle of 50° ($c = 0.022$) and is about 5.74%. Consequently, due to the insignificant effect of (c) on the intended results, we neglect this coefficient in equation (8).

Appendix 2

In the experimental method for deriving stress concentration factor (SCF), a test is first performed at 50° (see Figure 15), and an initial value is estimated for SCF based on the differences between green curve (asymmetric model without applying SCF) and red curve

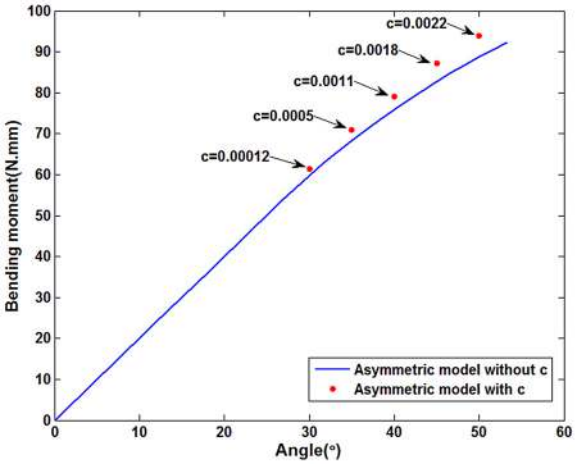

Figure 20. Effect of asymmetric coefficient (c) on the amounts of bending moment.

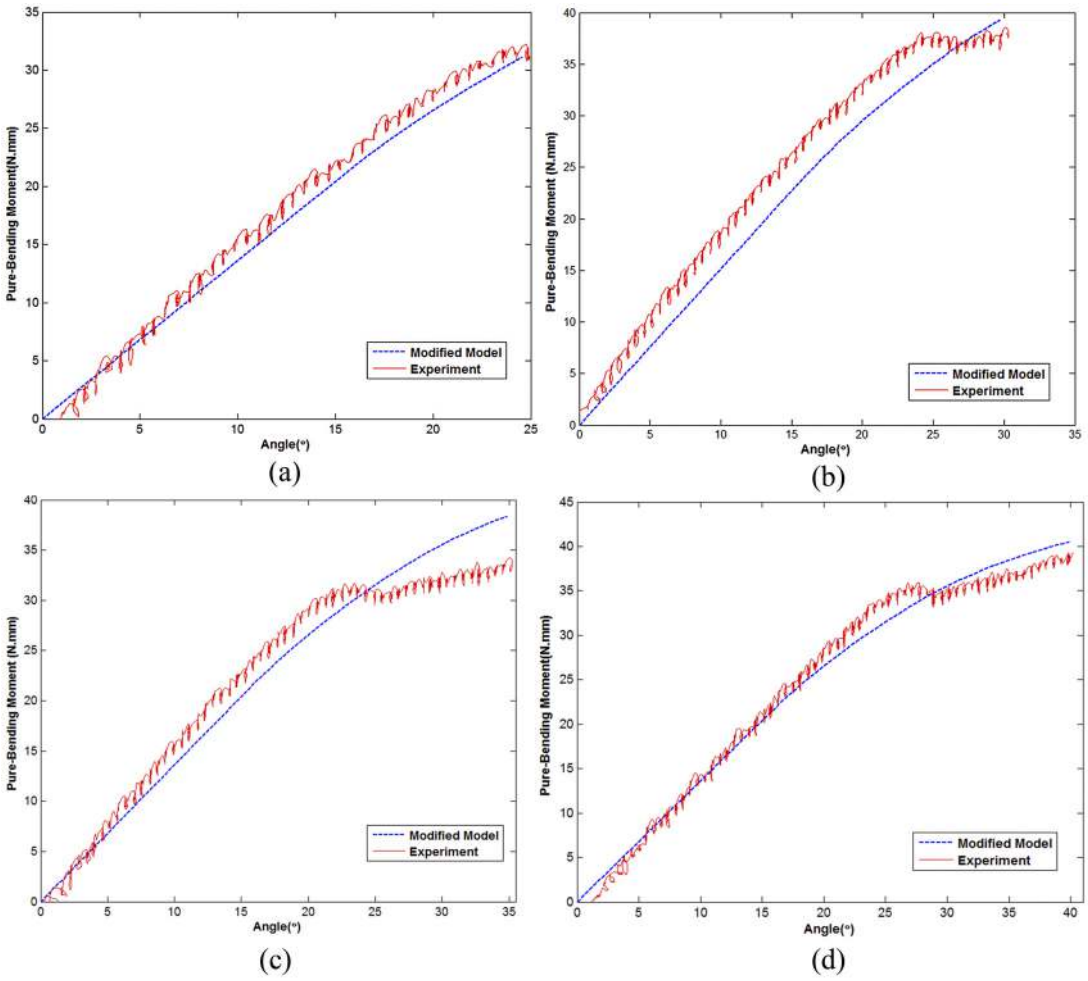

Figure 21. Comparison between experiments and the modified model for sample 1: (a) 25°, (b) 30°, (c) 35°, and (d) 40°.

(experiment). To validate the initial SCF value, four bending tests are performed in different angles (25°, 30°, 35°, and 40°) and the numerical model with the considered SCF is compared with the experiments. Figure 21 shows comparison between these two models for sample 1. Good agreements between two curves can verify the presented SCF values.